

4

THE DYNAMICS OF THE BROKEN RESONANCE CHAIN SYSTEMS AND THEIR FORMATION: THE SOLAR SYSTEM

In the past two decades, transit surveys have revealed a class of planets with thick atmospheres – sub-Neptunes – that must have completed their accretion in protoplanet disks. When planets form in the gaseous disk, the gravitational interaction with the disk gas drives their migration and results in the trapping of neighboring planets in mean motion resonances, though these resonances can later be broken when the damping effects of disk gas or planetesimals wane. It is widely accepted that the outer Solar System gas giant planets originally formed in a resonant chain, which was later disrupted by dynamical instabilities. Here, we explore whether the early formation of the terrestrial planets in a resonance chain (including Theia) can evolve to the present configuration. Using N-body simulations, we demonstrate that the giant planet instability would also have destabilized the terrestrial resonance chain, triggering moon-forming giant impacts in 20–50% of our simulated systems, dependent on the initial resonance architecture. After the instability, the eccentricity and inclination of the simulated planets match their present-day values. Under the proposed scenario, the current period ratio of 3.05 between Mars and Venus – devoid of any special significance in traditional late formation models – naturally arises as a relic of the former resonance chain.

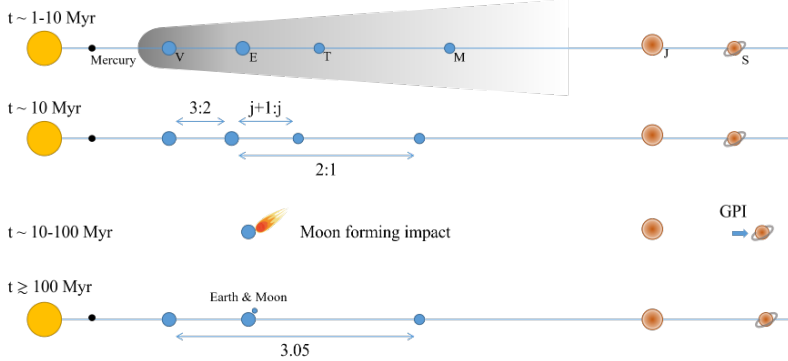


Figure 4.1. Sketch illustrating the dynamical evolution of the solar system planets during and after disk dissipation. The two-sided arrows represent the existence of mean motion resonances. Blue and brown scatters represent terrestrial bodies, including Venus (V), proto-Earth (E), Theia (T), and Mars (M), and gas giants including Jupiter (J) and Saturn (S). In the disk phase ($t \lesssim 1$ Myr), terrestrial planets form and migrate convergently. Theia and Earth are in $j + 1 : j$ resonance, where j is the resonance number. At $t \gtrsim 1$ Myr, i.e., just after disk dispersal, planets are still locked in a resonance chain. At $t \sim 10$ Myr, the outward migrating Saturn excites Jupiter, triggering the giant planet instability (GPI), which also destabilizes the resonance chain and triggers the moon-forming giant impact. After $t \sim 100$ Myr, the planets stabilize to the current architecture.

4.1 Introduction and motivation

If two planets are in a (first-order) orbital mean motion resonance, their period ratio stays close to an integer ratio, $j + 1:j$. Because the conjunction point occurs close to the pericenter of the inner and apocenter of the outer planet, the mean motion resonance enhances the dynamical stability of planetary systems (Tamayo et al. 2017; Goldberg et al. 2022). Mathematically, the resonance angles, which express the point where in the orbit conjunctions take place, are said to librate for planets in resonance. Examples in our solar system are the 1:2:4 resonance among Galilean moons and the 3:2 resonance between Neptune and Pluto. Many exoplanet systems are discovered to be in resonance as well, e.g., TRAPPIST-1 (Gillon et al. 2017; Luger et al. 2017), TOI-178 (Leleu et al. 2021), TOI-1136 (Dai et al. 2022), HD110067 (Luque et al. 2023). Planets in resonances are expected to experience large-scale migration, which is naturally explained by the formation of planets early, in a gas-rich disk (Papaloizou & Szuszkiewicz 2005). Exoplanet formation is widely believed to occur within protoplanetary disks, as supported by both observations (Andrews et al. 2018; Keppler et al. 2019; Barber et al. 2024) and theoretical models (Drążkowska et al. 2023; Mordasini et al. 2015). Efficient Type I migration often traps planets into mean motion resonances, as evidenced by the observed period ratio distributions in exoplanet populations (Huang & Ormel 2023; Hamer & Schlaufman 2024), particularly in young systems (Dai et al. 2024). In contrast, non-resonant planets with circulating resonance angles located near integer period ratios are much less stable (Hu et al. 2025).

Giant planets in our solar system are widely believed to start in a resonant configuration (Tsiganis et al. 2005). The resonance chain was then broken during giant planet instability (GPI, Liu et al. 2022; Griveaud et al. 2024; Brown et al. 2024). GPI is widely recognized as a turning point in the early evolution of our Solar System. In particular, such an event plays a key role in reproducing the observed orbital properties of the outer solar system bodies, such

Table 4.1. Orbital properties of Solar system planets (Murray & Dermott 1999). The planet mass, semimajor axis, orbital period, eccentricity, and inclination in the ecliptic and invariable planes are listed.

Name	$m_p [M_\oplus]$	$a_p [\text{au}]$	$P [\text{days}]$	e	Ecliptic i [deg]	Invariable i [deg]
Venus	0.82	0.72	224.7	0.0068	3.394	2.19
Earth	1.00	1.00	365.2	0.0167	0.000	1.57
Mars	0.11	1.52	687	0.0934	1.850	1.67
Jupiter	317.8	5.20	4331	0.0484	1.303	0.32
Saturn	95.2	9.57	10747	0.0541	2.485	0.93

as the eccentricities and inclinations of the giant planets (Tsiganis et al. 2005), distribution of the Kuiper Belt (Levison et al. 2008) and asteroid belt (O’Brien et al. 2007), Trojan asteroids of Jupiter and Neptune (Morbidelli et al. 2005), and irregular moons around giant planets (Nesvorný et al. 2014). However, the migration of giant planets during GPI not only affects their own orbits but also has profound consequences for any existing terrestrial planets. As Saturn migrates outward, it induces sweeping secular resonances that can perturb the orbits of inner planets, potentially triggering orbital crossing and collisions (Brasser et al. 2009; Kaib & Chambers 2016; Thommes et al. 2008).

Dynamical constraints indicate that the GPI occurred within 100 Myr after the formation of the Solar System (Nesvorný et al. 2018; de Sousa et al. 2020). This timing suggests that terrestrial planet formation was largely complete before the instability took place (Kobayashi & Dauphas 2013). Consequently, the terrestrial planets would have been in place when GPI perturbed their orbits, setting the stage for significant dynamical rearrangement and collisions. The most compelling evidence of such a collision in our inner Solar System must be the Moon-forming giant impact (Canup & Asphaug 2001). Cosmochemical studies constrain the Moon-forming event to have occurred between 40 and 120 Myr after Solar System formation (Barboni et al. 2017; Thiemens et al. 2019), which overlaps significantly with the estimated timing of the GPI. This temporal correlation has motivated studies suggesting that the dynamical disturbances associated with the GPI may have triggered the Moon-forming giant impact (Clement et al. 2023). Specifically, in their model terrestrial planets form after gas dispersal by collisional growth between Mars-sized embryos (Clement et al. 2019).

It is still under debate whether terrestrial planets largely complete their growth early in the protosolar nebulae, when gas was still present (Johansen et al. 2024; Morbidelli et al. 2024). Here we hypothesize that the terrestrial planets in our Solar System formed early in the protosolar nebulae—a scenario supported by both formation models (Johansen et al. 2021; Brož et al. 2021) and observational work on Mars isotopes (Kobayashi & Dauphas 2013) and Earth oxidation state (Young et al. 2023; Johansen et al. 2023). Naturally, planets can get trapped in resonance due to disk migration. However, it remains unclear whether the observed architecture of the terrestrial planets can be reproduced starting from an initial resonance chain. To investigate this hypothesis, this work initializes terrestrial planets in a resonance chain. Their long-term dynamical evolution is tracked and studied.

The paper is structured as follows. We detailed the methodology in Sect. 6.2. Our main results and their comparison to the present solar system are in Sect. 6.3. The implications of our findings are discussed in Sect. 4.4. Finally, we state our conclusions in Sect. 6.6.

4.2 Model

We illustrate the dynamical evolution of terrestrial planets in Fig. 4.1 over time. In our setup, we include four terrestrial planets—Venus, proto-Earth, Theia, and Mars—in resonance. We exclude Mercury from the resonance chain because of its potentially distinct formation history compared to the other terrestrial planets (e.g. Johansen & Dorn 2022; Morbidelli et al. 2022). Mercury is also very far from other terrestrial planets, interior to the 3:1 period ratio of Venus. Including it would not affect the current results due to the very low mass of Mercury (half that of Mars). Besides, Mercury seems to experience more complex dynamical interaction with the Sun, as evidenced by the 3:2 spin-orbit resonance (e.g. Wieczorek et al. 2012; Noyelles et al. 2014).

In addition, we include two gas giants, Jupiter and Saturn, initially arranged more compactly than observed today with a period ratio smaller than 2, and Saturn migrates outward to its present orbit (Morbidelli et al. 2007; Levison et al. 2011). During this migration phase (giant planet instability), Jupiter’s eccentricity is excited at various resonance locations, and the terrestrial planets experience secular perturbations from the giant planets (Brasser et al. 2009; Kaib & Chambers 2016).

In our scenario, the terrestrial resonance chain is broken during Saturn’s outward migration, leading to increased eccentricities among the terrestrial planets. The Moon-forming giant impact is then triggered once the orbits of proto-Earth and Theia overlap. Since Venus and Mars are relatively distant from their neighboring terrestrial planets, their orbits remain largely unchanged, thereby preserving the initial 3:1 period ratio between Mars and Venus, which is consistent with current observations.

We use the REBOUND (Rein & Liu 2012) package to conduct the N-body calculations. The migration and eccentricity damping forces are implemented using REBOUNDx (Tamayo et al. 2020) and the MERCURIUS integrator (Chambers 1999; Rein et al. 2019) is employed.

4.2.1 Initial conditions

The terrestrial planets are initially set in resonance in our N-body simulations. In our model, Venus reaches the migration barrier, possibly the disk inner edge, which promotes convergent migration and thus resonance trapping (see Fig. 4.1). To achieve these initial resonant conditions, we follow the approach of (Tamayo et al. 2017): we first position the planets slightly away from exact resonance and then allow convergent migration to capture them into resonance while damping their eccentricities. The acceleration term due to the gravitational interaction with the disk used in our N-body calculations is

$$\mathbf{F}_i = \frac{\mathbf{v}_i}{2\tau_{a,i}} + \frac{2(\mathbf{v}_i \cdot \mathbf{r}_i)\mathbf{r}_i}{r_i^2\tau_{e,i}}, \quad (4.1)$$

where \mathbf{v}_i and \mathbf{r}_i denote the velocity and position vector of planet i , and $\tau_{a,i}$ and $\tau_{e,i}$ are the semimajor axis and eccentricity damping timescale. Venus migrates outward on a timescale τ_a of 10 Myr. Such a long timescale represents the end stage of the disk environment. Planet eccentricities are damped on a timescale of $\tau_e = \tau_a/K_e$, where K_e is a free parameter ranging from 10^2 to 10^4 . The parameter K_e controls the eccentricities of the terrestrial planets in the resonance chain (Tanaka & Ward 2004). Large K_e leads to smaller eccentricities.

The simple migration setup described above ensures convergent migration and, consequently, resonance trapping in a controlled manner. In reality, however, the process of resonance trapping is more complex. Convergent migration may occur, for instance, if Venus

halts its migration at the migration barrier of the protoplanet disk (Liu et al. 2022; Ogihara et al. 2024; Wu & Chen 2025). The detailed processes by which terrestrial planets form and migrate within the disk remain uncertain but do not matter for this study as long as the terrestrial planets end up in the resonance chain depicted in Fig. 4.1.

Jupiter and Saturn are also included in the simulation. Jupiter is initialized at its present-day orbital period with eccentricity $e_{J,\text{ini}}$ ranging from 0 to 0.05, and an inclination of 0.5 degrees. Saturn is placed at an initial period ratio of 1.9 with Jupiter, i.e., closer to Jupiter than at present and within the 2:1 resonance location.

Most simulations succeed in forming a resonance chain, characterized by the libration of resonance angles among the terrestrial planets. We consider the point when Venus has migrated to 0.72 au (the current location of Venus) as the initial conditions for the post-disk dynamical evolution.

4.2.2 Giant planet instability

During the phase of giant planet instability, Saturn migrates outward. The driven process and the timescale of such migration are still under active debate (Liu et al. 2022; de Sousa et al. 2020; Agnor & Lin 2012). We therefore parameterize Saturn's migration with the additional acceleration term in the N-body calculation:

$$F = \frac{1}{2} \frac{a_0 - a_f}{a} \frac{v}{\tau_s} e^{-t/\tau_s}, \quad (4.2)$$

where a_0 and a_f are the initial and expected final positions of the body, a and v are the semi-major axis and velocity of the migrating body, and τ_s controls the timescale of the migration. It results in the semimajor axis changing in the form of $a(t) = a_f + (a_0 - a_f)e^{-t/\tau_s}$ (Brasser et al. 2009; Kaib & Chambers 2016; Fang et al. 2025). Such exponential migration has been implemented in REBOUNDx by Ali-Dib et al. (2021). We run simulations varying the outward migration timescale of Saturn τ_s from 0.8 to 16 Myr. The solar system is integrated for 100 Myr. The parameter sensitivity is discussed in Appendix ??

4.2.3 Theia and proto-Earth mass-radius calculation

After Theia collides with proto-Earth, the resulting merger—the Earth-Moon system—is located at the center of mass of the two original bodies. Since Earth currently orbits at 1 au, we fix the center of mass at 1 au in our setup, meaning that different initial configurations for Earth and Theia yield different planet mass ratios.

Assuming a perfect merger and small eccentricities, angular momentum conservation gives:

$$m_E \sqrt{a_E} + m_T \sqrt{a_T} = (m_E + m_T) \sqrt{a_\oplus}. \quad (4.3)$$

The "E" and "T" notations are for proto-Earth and proto-Theia, while \oplus notation is for the present-day Earth. After inserting values, we find

$$m_T = m_E \frac{\sqrt[3]{\frac{2P_\oplus}{3P_V}} - 1}{\sqrt[3]{\frac{j+1}{j}} - \sqrt[3]{\frac{2P_\oplus}{3P_V}}} = m_E \frac{0.0272}{\sqrt[3]{\frac{j+1}{j}} - 1.0272} \quad (4.4)$$

where j is the resonance number of proto-Earth and Theia. When $j = 4$, $m_T = 0.54m_E$. when $j = 3$, $m_T = 0.37m_E$. We assume $m_E + m_T = 1.05m_\oplus$ in all of our calculations. Venus and Mars

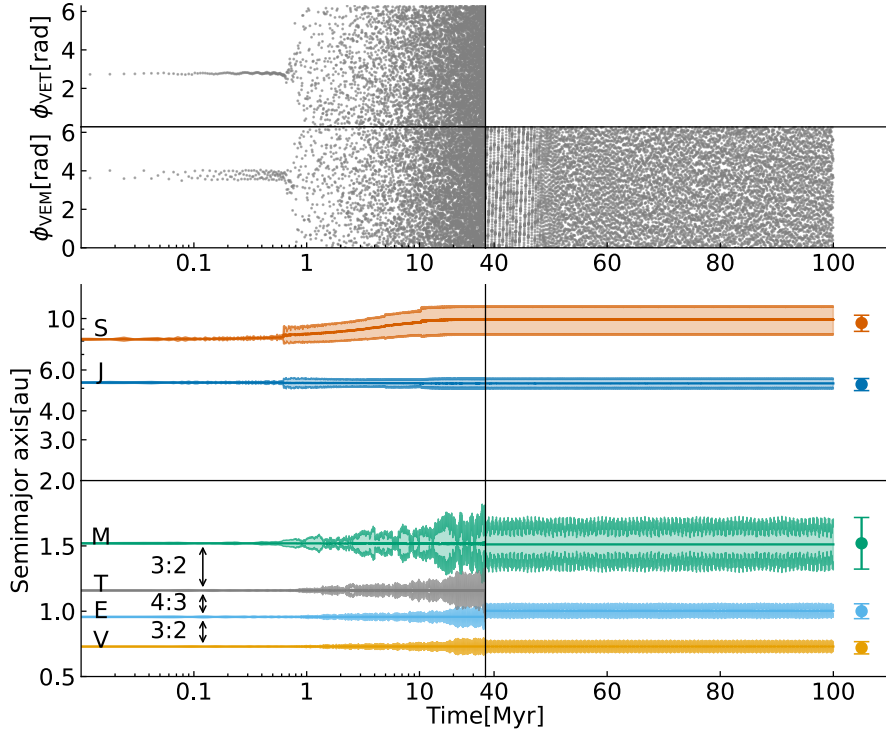


Figure 4.2. Dynamical evolution of planets during Saturn’s outward migration and the post-Moon-forming impact phase. The top panel shows the evolution of 3-body resonance angles of Venus, Earth, and Theia (ϕ_{VET}) and Venus, Earth, and Mars (ϕ_{VEM}). The resonance angles are defined in Sect. 6.3. The bottom panel shows the changes of planet semimajor axis and eccentricity with time. The curves show the orbital evolution of each body, including its semi-major axis (thick), perihelion, and aphelion (thin). The terrestrial planets are initially in a resonance chain. The corresponding resonances are labeled by the double-headed arrows. The semimajor axis, aphelion, and perihelion of the current solar system planets are denoted by the error bars at the right. The adopted parameters are: $e_{J,\text{ini}} = 0.005$, $\tau_S = 4.7$ Myr and $K_e = 5.6 \times 10^3$. The crossing of the 2:1 resonance between Saturn and Jupiter (≈ 1 Myr) also destabilizes the inner solar system, breaking its resonances and resulting in the Moon-forming event (≈ 35 Myr).

do not experience giant impacts as suggested for Earth, and their mass does not change in our model.

Planets collide if their physical radii overlap. Planet radii are adopted from current measurements, except for proto-Earth and Theia, which no longer exist in the present Solar System. For bodies with masses below $1 m_\oplus$, we use the mass-radius relationship

$$\frac{R}{1 R_\oplus} = \left(\frac{m}{1 m_\oplus} \right)^{0.29} \quad (4.5)$$

as given in (Seager et al. 2007), which employs a polytropic model to describe the internal structure of rocky planets. The adopted planet properties are summarized in Table 4.1.

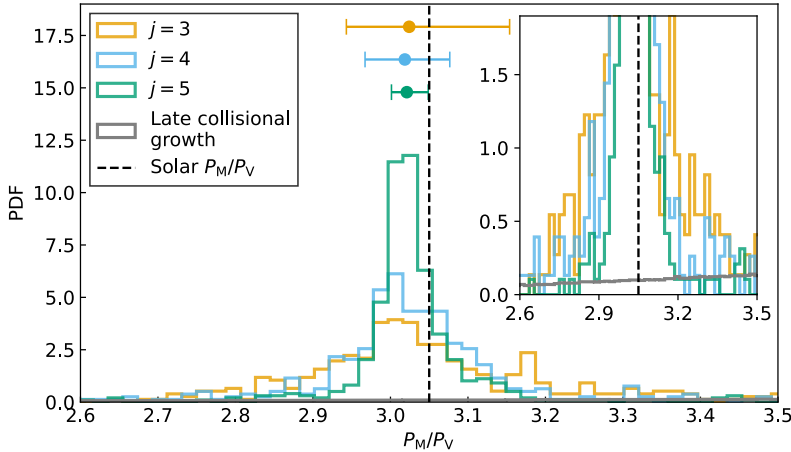


Figure 4.3. Mars-Venus period ratio probability distribution from different models. The current value is shown by the vertical dashed line. The colored histograms are the subgroup of simulated systems (defined in Fig. 4.7) of the early, resonant, formation models, with different colors representing the Theia and Earth resonances through the resonance number j . The corresponding median 50% ranges and the median values are indicated by the error bars and their center values. The grey histograms are the results of the post-nebulae collisional growth model, which does not feature an elevated probability near the 3:1 period ratio (see Appendix ??). The figure inset features a shorter range of the y-axis

4.3 Comparison with Solar system

Firstly, we hypothesize that the four terrestrial planets—Venus, Earth, Theia, and Mars—emerged from the gaseous disk in a 2:3:4:6 resonance chain. We find that this resonant architecture is a natural consequence regardless of whether planet formation proceeds via pebble accretion or planetesimal accretion (see Appendix ??). This resonance chain guarantees a 3:1 period ratio between Mars and Venus. Due to their close spacing, Theia and proto-Earth are prone to collide once the resonance is broken, giving rise to the Earth-Moon system at 1 au. Consequently, the mass ratio between Theia and proto-Earth is based on their initial positions; with Venus fixed at its current distance of 0.72 au, the mass ratio amounts to 0.37 (see Eq. (4.4)).

It was constrained that the giant planet instability occurred in the first 10 – 100 Myr after the formation of Calcium-aluminum-rich Inclusions (CAIs) (Edwards et al. 2024). This instability may be triggered either by gas disk dissipation (Liu et al. 2022; Thommes et al. 2008), by self-driven dynamical processes (de Sousa et al. 2020; Griveaud et al. 2024), or even by stellar encounters (Portegies Zwart et al. 2021; Brown et al. 2024). In our simulations, we simply migrate Saturn outward, following approaches used in previous studies (Brasser et al. 2009; Kaib & Chambers 2016; Fang et al. 2025). The timescale of Saturn’s outward migration, τ_S , is parameterized between 0.8 and 16 Myr (Liu et al. 2022; Griveaud et al. 2024). Although the dynamical instability of the giant planets has shaped many other features of the outer Solar System (e.g. Tsiganis et al. 2005; Morbidelli et al. 2005; Ormel & Huang 2025), here we focus on its effect on the architecture of the terrestrial planets.

Figure 4.2 illustrates a representative simulation in which the primordial resonance chain is broken by the migrating Saturn. Initially, both 3-body resonance angles, which are composed of the mean longitudes of relevant planets ϕ_{VET} and ϕ_{VEM} librate, where $\phi_{VET} =$

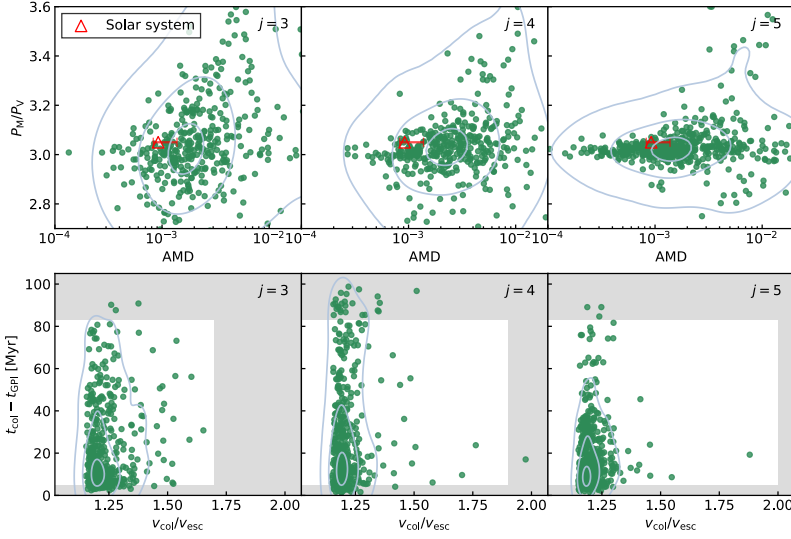


Figure 4.4. Planet properties for the simulated Solar-like systems in which Theia collides with Earth. The definition of Solar-like system is in Fig. 4.7. Each simulation starts with a terrestrial resonance chain and two gas giants. Theia and Earth are initially in $j+1:j$ resonance, with the resonance number $j=3, 4$, or 5 labeled on the top right of each panel. The top panels show the Angular Momentum Deficit (x-axis) and Mars-Venus period ratio (y-axis). The present-day Solar System is marked by a triangle for comparison, while the error bar shows the range in secular evolution (Ito & Tanikawa 2002). The bottom panels show Theia’s collision velocity with Earth in terms of the escape velocity (x-axis) and the collision time with respect to the GPI (y-axis). Permissible cosmochemical constraints on the timing (Barboni et al. 2017; Thiemens et al. 2019) of the GPI and SPH simulation constraints on the impact velocity of the Moon-forming event (Timpe et al. 2023) are indicated by the white window, in which the GPI is assumed to occur at 37 Myr after CAI (de Sousa et al. 2020).

$2\lambda_V - 6\lambda_E + 4\lambda_V$ and $\phi_{VEM} = 2\lambda_V - 4\lambda_E + 2\lambda_M$. In our model, Jupiter’s eccentricity is excited to approximately $e_J \approx 0.05$ as Saturn crosses the 2:1 resonance (Lithwick et al. 2012). Subsequently, the g_5 secular resonance (Brasser et al. 2009) sweeps through the terrestrial planets’ orbits and the angular momentum deficit (AMD) – a measure of the dynamical excitation of the system (Laskar 1997) – diffuses (Kaib & Chambers 2016), disrupting their resonant configuration. With circulating resonance angles planets are no longer in resonance, but remain near integer period ratios. In addition to the secular perturbations from Jupiter, close encounters among near-resonant terrestrial planets further amplify planet eccentricities, leading to orbital overlap between Theia and Earth, culminating in their collision. Following the Moon-forming event, the terrestrial orbits stabilize as they are displaced away from both secular and mean-motion resonances. Although the semi-major axes remain essentially constant, the eccentricities continue to librate under Jupiter’s secular influence (Murray & Dermott 1999). Overall, our simulation reproduces the orbital properties of the present-day terrestrial planets.

Perhaps the most direct quantity to compare the simulated systems with the current Solar System is the period ratio between Venus and Mars, which is observed to be $P_M/P_V = 3.057$. We compile the period ratios from our simulations across different parameter sets. The statistics of simulated systems, such as displayed in Fig. 4.3, include only those simulations in which Jupiter’s free and forced eccentricities match their present-day values. See appendix ??

(Fig. 4.7) for discussion on how this selection was made. All other figures in the main text are also based on this conditional subset. The probability distribution of P_M/P_V peaks at approximately 3.01, consistent with the planets' pre-instability configuration—a value that arises from the balance between planet migration and eccentricity damping (Charalambous et al. 2022). Due to planet-planet scattering during the simulation, the distribution broadens from a δ -function, with the observed period ratio falling within the 25% range from the median. For comparison, we also overplot the period ratio distribution from the late formation model (see Fig. 4.11 in Appendix ??), in which terrestrial planets grow via mutual giant impacts between planet embryos. Compared to the late formation model, the early formation scenario yields a probability density higher by more than an order of magnitude of reproducing the observed Mars-Venus period ratio. The zoomed-in version of the period ratio distribution in the late formation scenario is also shown, in the subset.

We also run two additional sets of simulations, varying the resonant configurations of Theia and proto-Earth by initializing them in a 4:5 mean-motion resonance (MMR, $j=4$) and a 5:6 MMR ($j=5$), while preserving the 2:3:6 resonance chain among Venus, proto-Earth, and Mars to maintain the 3:1 period ratio between Mars and Venus. In each case, we recalculate the mass ratio of Theia-toproto-Earth to ensure that their center of mass remains at 1 au. As the resonance index j increases, Theia's mass also increases. The resulting Mars-Venus period ratios are shown in Fig. 4.3 (blue and green lines). When Theia starts in a closer orbit to Earth (i.e., with a higher j value), the spread of the period ratio distribution narrows. This occurs because a more massive Theia is less susceptible to excitation and remains closer to Earth, making it more difficult to perturb Mars. Consequently, the simulated Mars-Venus period ratio exhibits a stronger peak around 3.01, although the observed value still falls within the quartile range of the distribution. Later dynamical processes could further adjust the planet positions. For example, the ≈ 0.05 wt% late veneer accreted by Mars (Brasser et al. 2016) may have slightly shifted its orbit outward.

Apart from the period ratio, we used another system-level indicator to test whether our simulated systems are consistent with the global properties of the Solar System – the Angular Momentum Deficit (AMD)

$$\text{AMD} = \frac{\sum_j M_j \sqrt{a_j} (1 - \sqrt{1 - e_j^2} \cos i_j)}{\sum_j M_j \sqrt{a_j}}. \quad (4.6)$$

Our simulation results match the Solar System well. As shown in Fig. 4.4 (top panels), the solar system resides within the central 10% of the distribution derived from our simulations. The higher eccentricity of Jupiter (grey scatter) results in systems with larger terrestrial AMD. A more direct approach is to individually compare each planet's eccentricity and inclination. As demonstrated in Fig. 4.8, the terrestrial planets in our simulations exhibit eccentricities and inclinations similar to those observed in the present-day Solar System.

The simulated planet systems exhibit a wide range of dynamical outcomes. In our simulations, Theia does not always collide with Earth; it may instead impact Mars, or if the system becomes too dynamically excited, it may lead to multiple planet collisions. Conversely, in some simulations, the planets remain on their initial orbits with minimal excitation, or they become over-excited to high inclinations that no collisions occur at all. Figure 4.5 presents the statistical distribution of these outcomes. The desired scenario—Theia colliding with Earth—occurs in 20–50% of simulated systems, depending on the initial resonant configuration (j). Naturally, placing Theia in a mean-motion resonance (MMR) closer to Earth promotes orbital overlap between the two bodies, while simultaneously reducing the probability of Theia impacting Mars.

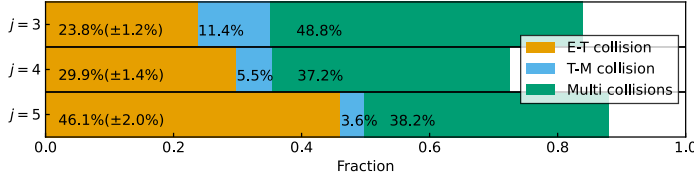


Figure 4.5. Statistical outcomes of simulated Solar-like systems, with final Jupiter eccentricities similar to the present day value (Fig. 4.7). The architecture of simulated systems is classified into four groups: Theia collides with Earth (orange); Theia collides with Mars (blue); There are multiple collisions (green); No collisions occur (white). The fractions of different types of simulated Solar systems are stated, where for the Earth-Theia collision case the Poisson error is also stated. Different j values (y-axis) represent different initial resonance configurations between Earth and Theia.

It is commonly accepted that the Moon was formed through a giant impact (Canup et al. 2023). We record the time of the Theia-Earth impact in our simulations in Fig. 4.4. About 50% of our simulated systems have Theia and Earth colliding within 30 Myr. Since our simulations start with the onset of giant planet instability (GPI), the absolute time (w.r.t CAI formation) of the Theia-Earth collision needs to be corrected accordingly. Dynamical evidence of Kuiper belt objects in our solar system shows that the GPI occurs at 37–62 Myr after CAI (de Sousa et al. 2020). Assuming GPI occurs at 37 Myr, then the simulated Theia and Earth collide at ≈ 67 Myr w.r.t CAI formation. Such timing is consistent with the cosmochemical constraints that the Moon-forming giant impact is at 40–120 Myr (Barboni et al. 2017; Thiemens et al. 2019).

In the canonical model of the Moon-forming event, a Mars-sized body collides with proto-Earth, delivering the angular momentum required for the Earth-Moon system (Canup & Asphaug 2001). However, the isotopic similarities between the Earth and the Moon (Wiechert et al. 2001) suggest that either the impactor had nearly the same composition as Earth or, more naturally, that the collision was highly energetic. For this reason, a scenario with a more massive impactor has recently emerged as a promising alternative (Lock et al. 2018; Asphaug et al. 2021), which also guarantees a sufficiently massive proto-lunar disk (Timpe et al. 2023). In our model, the mass ratio γ between Theia and proto-Earth is 0.37, 0.54, and 0.76 for the initial 4:3, 5:4, and 6:5 Theia-Earth resonances, respectively. Given these mass ratios, the collision velocity is constrained to $\lesssim 1.5v_{\text{esc}}$, where v_{esc} is the mutual escape velocity of the target and impactor (Timpe et al. 2023; Asphaug et al. 2021). As shown in Fig. 4.4, our simulated systems exhibit relatively low impact velocities because the resonance configuration allows the planets to be closely spaced initially. These modest impact velocities are in line with the aforementioned constraints in the scenario of a more massive Theia than the canonical model.

4.4 Implications

The implication of our model is that proto-Earth formed early, which has been argued to be inconsistent with the observed Hf-W isotope system in bulk silicate Earth (BSE) (Morbidelli et al. 2024). This occurs because, during core formation, the lithophile parent element ^{182}Hf remains in the mantle, leading to an excess of its decay product ^{182}W relative to present-day measurements (Olson et al. 2022). However, several factors could operate to decrease the relative abundance of ^{182}W in the Earth's mantle. For example, an effective equilibration

between the iron core and the mantle after the Moon-forming event (Deguen et al. 2011), the late accretion of $\sim 10\%$ planetesimals (Olson & Sharp 2023), or multiple collisions in a hit-and-run scenario (Asphaug et al. 2021), would reduce the concentration ^{182}W in the mantle. Because Venus never experienced violent impact events such as the Moon-forming giant impact in our model, we expect the Venus mantle to be largely primordial, with a much higher ^{182}W abundance than in Earth's mantle.

An early formation scenario, as proposed here, would resolve the challenges posed by the later formation model. These include: 1) The absence of a moon for Venus is puzzling (Asphaug et al. 2021; Malamud & Perets 2024), giving the prevalence of giant impacts in the late accretion model (Jacobson et al. 2014). 2) The need for post-impact damping mechanisms (Clement et al. 2023), such as by leftover planetesimals, to reduce the eccentricities to their observed values (Hansen 2009). Collisional growth also results in random orientation of the spin axis (Chambers 2001; Miguel & Brunini 2010), inconsistent with solar terrestrial planets. 3) The magma ocean may exist and prevent the formation of an early and stable crust due to the frequent collisions in the late collisional growth scenario, inconsistent with the early crust on Earth (Harrison 2009).

Mars grew up in the first 1-10 Myr (Dauphas & Pourmand 2011; Kobayashi & Dauphas 2013; Marchi et al. 2020; Woo et al. 2021), contemporaneous with the lifetime of the gaseous protoplanetary disk (Weiss et al. 2021). There are no fundamental reasons why growth for the other terrestrial planets would have been stalled at Mars size. Mature exoplanets are widely believed to be formed in the gas disk (Drążkowska et al. 2023; Mordasini et al. 2015), as evidenced by the detections of young planets (David et al. 2019; Keppler et al. 2019; Barber et al. 2024; Dai et al. 2024).

Yet $>80\%$ of those found by Transit (using Kepler and TESS) are not in resonance (Huang & Ormel 2023; Hamer & Schlaufman 2024). Various scenarios have been proposed to explain the overall observed non-resonant planetary architecture statistically, due to dynamical instability triggered by disk dispersal (Izidoro et al. 2021), and planet-planet scattering (Wu et al. 2024; Li et al. 2024). Recently, radial velocity follow-up studies have revealed the existence of outer gas giant(s) to systems hosting inner planets with irregular architecture (He & Weiss 2023). This finding aligns with the scenario that an external perturber destroyed the inner resonance architecture. Scenario similar to the one proposed here for the Solar System could therefore have been common in the evolution of exoplanet systems (Yi et al. 2025). Notably, no outer giant planet has yet been observed in evolved resonance chain systems (e.g., TRAPPIST-1 Boss et al. 2017).

4.5 Conclusions

We hypothesize that terrestrial planets (including Theia) in our Solar system formed early in the protosolar nebula. Naturally, they are trapped in a resonance chain. Starting with the resonant configuration, we use N-body simulations to study the destabilization of the resonance chain and long-term evolution. During the evolution, Theia commonly collided with proto-Earth (at a rate $20 \sim 50\%$, depending on the initial resonance between Earth and Theia). A comparison with the properties of Solar System terrestrial planets shows that our model satisfies four key constraints:

1. The Mars-Venus period ratio of 3.05 is a relic of the former resonance chain. This value arises naturally in the early formation scenario, with a probability density an order of magnitude higher than in the late formation model (Fig. 4.3).

2. The resulting planet eccentricities and mutual inclinations are moderate in the simulated systems. Their values are consistent with the current solar system (Fig. 4.4 upper panels and Fig. 4.8). No post-moon forming damping is required.
3. The impact velocity between Earth and Theia is always $\lesssim 1.5$ of the escape velocity (Fig. 4.4 lower panels) in our simulated systems, consistent with the Moon-forming giant impact (Timpe et al. 2023).
4. The Earth-Theia giant impact follows the onset of giant planet instability, and occurs $\gtrsim 10$ Myr afterwards (Fig. 4.4 lower panels). It is in line with cosmochemical dating.

Two immediate predictions follow from our investigation. First, a giant impact event with Venus is disfavored in our model. Therefore, its mantle composition stays largely primordial, and we expect its isotopic signature to reflect early formation. Future missions characterizing isotopic abundances on Venus would offer the opportunity to verify the early formation models for the Solar terrestrial planets in this work.

Second, most exoplanets are not in resonance. They may start in resonance but later get destabilized. We demonstrate that the outer massive companion can destroy the resonance chain. Our dynamical study hints that those exoplanet systems that harbor evolved long resonance chains are unlikely to host external gas giants.

Appendix

4.A Formation of a resonant chain in the pebble accretion and planetesimal accretion models

We employ simplified planet formation models to demonstrate that the initial resonant architecture of the terrestrial planets is feasible. In Fig. 4.6, we show that both pebble accretion and planetesimal accretion can produce a resonant configuration within a gaseous disk—the starting condition for our study. In the pebble accretion scenario, planet embryos are introduced sequentially at the water iceline, then grow and migrate inward one after another. In contrast, the planetesimal accretion scenario initializes embryos simultaneously at different orbital distances. Ultimately, these processes yield a 2:3:4:6 resonance chain corresponding to Venus, Earth, Theia, and Mars. Notably, the final resonant architecture depends on the time interval (for pebble accretion) or spatial separation (for planetesimal accretion) between adjacent planet pairs. To achieve a tighter resonance between Theia and Earth, the interval between the initial Earth and Theia embryos must be reduced.

In the following, we detail the models and the parameter choices used for planet formation. We fix the gas disk surface density distribution at:

$$\Sigma_g = \Sigma_{g,0} f_g \left(\frac{r}{1 \text{ au}} \right)^{\beta_0} \left(1 - \sqrt{\frac{r}{R_{\text{in}}}} \right) e^{-\left(\frac{r}{R_{\text{out}}} \right)^{2-\beta_0}}, \quad (4.7)$$

where $\Sigma_{g,0} = 2400 \text{ g/cm}^2$ is the surface density in the minimum-mass solar nebulae (MMSN), $f_g = 5$ is the scaling factor of the initial gas surface density with respect to MMSN, $R_{\text{out}} = 30 \text{ au}$ is the disk outer radius, and $\beta_0 = -1.5$ is the surface density power law index. The disk inner radius is set to be $R_{\text{in}} = 0.6 \text{ au}$, which prevents Venus from migrating further inward. Such an effective inner disk edge (migration barrier) could be triggered by the wind-driven accretion increasing with time (Ogihara et al. 2024; Wu & Chen 2025). It ensures the

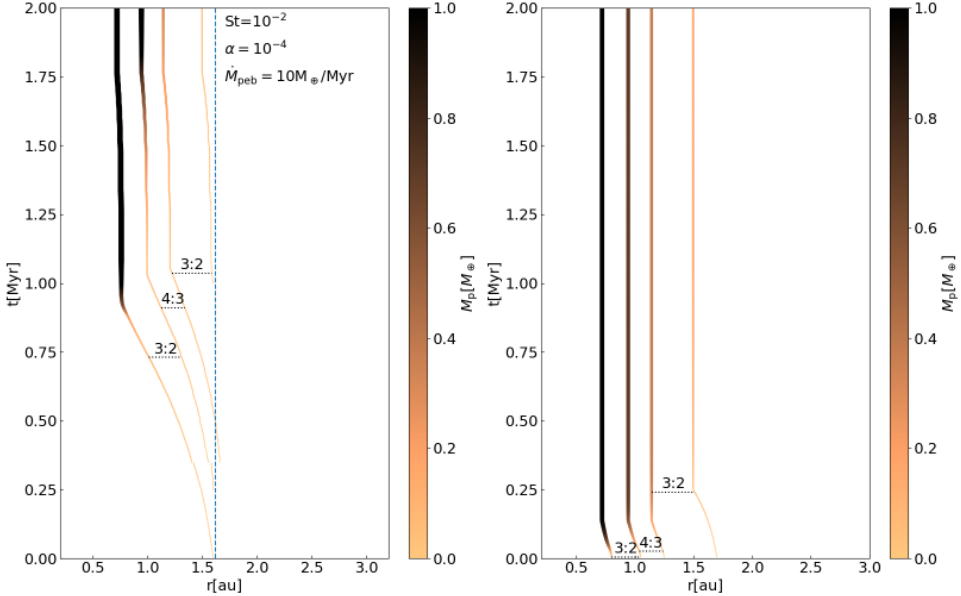


Figure 4.6. Simulations of planetary accretion and migration, illustrating the formation of resonant architectures. The left panel shows planets growing via pebble accretion, while the right panel depicts growth through planetesimal accretion, both occurring within a gaseous protoplanetary disk. In each panel, the trajectories represent the evolution of the semimajor axis (x-axis) and planetary mass (copper color) over time (y-axis). They denote, from left to right, Venus, Earth, Theia, and Mars. In the left panel, the vertical blue line marks the water snowline.

convergent migration of terrestrial planets (Brož et al. 2021; Clement et al. 2021). The disk temperature profile is fixed at

$$T = T_0 \left(\frac{r}{1 \text{ au}} \right)^{\xi_0}, \quad (4.8)$$

we take the temperature power law index $\xi_0 = -0.5$ and the temperature at 1 au $T_0 = 200$ K.

For type-I migration, we use,

$$\dot{r} = -k_{\text{mig}} \frac{m}{m_{\star}} \frac{\Sigma_g r^2}{h^2} h^{-2} v_K, \quad (4.9)$$

where \dot{r} is the shrinking rate of the planet's semimajor axis, h is the disk aspect ratio, and we take the mean molecular weight as 2.4. The prefactor k_{mig} depends on the disk properties. We adopt the fit from D'Angelo & Lubow (2010),

$$k_{\text{mig}} = 2(1.36 - 0.62\beta - 0.43\xi), \quad (4.10)$$

where β and ξ are the local gradient indices of disk surface density and temperature. As the two adjacent planets convergently migrate to the resonance location, they get trapped with their periods near integer commensurability.

If planets grow by pebble accretion (Fig. 4.6 left panel), we can get the accretion rates of the planet via

$$\dot{m} = \epsilon \dot{M}_{\text{solid}}, \quad (4.11)$$

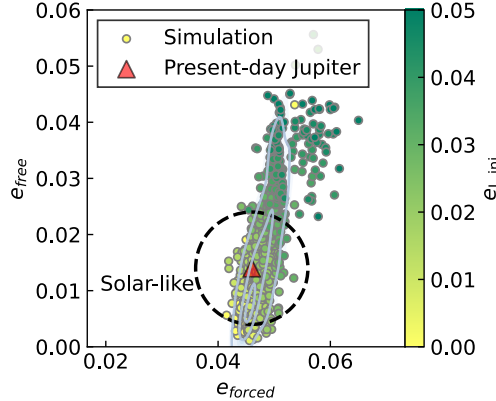


Figure 4.7. Jupiter's free and forced eccentricities obtained at the end of the simulations. The scatters with different colors are the results of the simulations starting with different initial Jupiter eccentricities. The solar system is marked as a triangle. The scatters in the circle (of radius 0.01) are indicated as the Solar-like systems in the simulation because they have similar Jupiter eccentricities as the present-day Jupiter.

The 3D pebble accretion efficiency ϵ is calculated following Ormel & Liu (2018). It depends on the planet's eccentricity, the particle Stokes number St , the local gas pressure gradient η , the disk aspect ratio h , and the gas turbulent diffusion parameter α_t . The quantities h and η follow from the disk structure. We assume zero eccentricities, fix $St=0.01$ and $\alpha_t = 10^{-4}$, and assume an incoming pebble mass flux of $\dot{M}_{\text{dust}} = 10 m_{\oplus} \text{ Myr}^{-1}$.

One of our simulation results is shown in Fig. 4.6 left panel. Similar to Johansen et al. (2021), we initialize four planet embryos at the iceline sequentially. They grow and migrate inward one by one. Venus stops its migration at 1 Myr because it reaches the migration barrier (Ogihara et al. 2024; Wu & Chen 2025). As the latter planets join, they form a 2:3:4:6 resonance chain. Their mass also increases after the formation of a resonance chain due to pebble drift in the disk. At the end of the simulation time (2 Myr), all four planets have their mass close to the present values.

Alternatively, if planets grow up from accreting planetesimals (Fig. 4.6 right panel), the planet oligarchic growth timescales follow from (Kokubo & Ida 2002)

$$\tau_p = 1.2 \times 10^5 \text{ yr} \left(\frac{\Sigma_{\text{plts}}}{10 \text{ g cm}^{-2}} \right)^{-1} \left(\frac{r}{1 \text{ au}} \right)^{\frac{3}{5}} \left(\frac{m}{m_{\oplus}} \right)^{\frac{1}{3}} \left(\frac{\Sigma_g}{2400 \text{ g cm}^{-2}} \right)^{-\frac{2}{5}} \left(\frac{m_{\text{plts}}}{10^{18} \text{ g}} \right)^{\frac{2}{15}}, \quad (4.12)$$

where m is planet mass, the mass of a planetesimal m_{plts} is fixed to be 10^{18} g, equivalent to a diameter of ≈ 6 km for an internal density of 1 g/cm^3 . The initial planetesimal disk surface density distribution Σ_{plts} follows a similar shape as the gas disk in Eq. (4.7),

$$\Sigma_{\text{plts}} = 90 \text{ g/cm}^2 \left(\frac{r}{1 \text{ au}} \right)^{\beta_{\text{plts}}} \left(1 - \sqrt{\frac{r}{R_{\text{in}}}} \right) \exp \left[- \left(\frac{r}{R_{\text{out}}} \right)^{2-\beta_{\text{plts}}} \right], \quad (4.13)$$

but with most of the planetesimal concentrated at ~ 1 au by using a much steeper gradient value $\beta_{\text{plts}} = -5.5$. Such a ring-like distribution of planetesimals is advantageous for forming a small Mars, aligning with the previous findings (Woo et al. 2024). Similar to Emsenhuber et al. (2021), we subtract the accreted planetesimal mass from the planetesimal surface den-

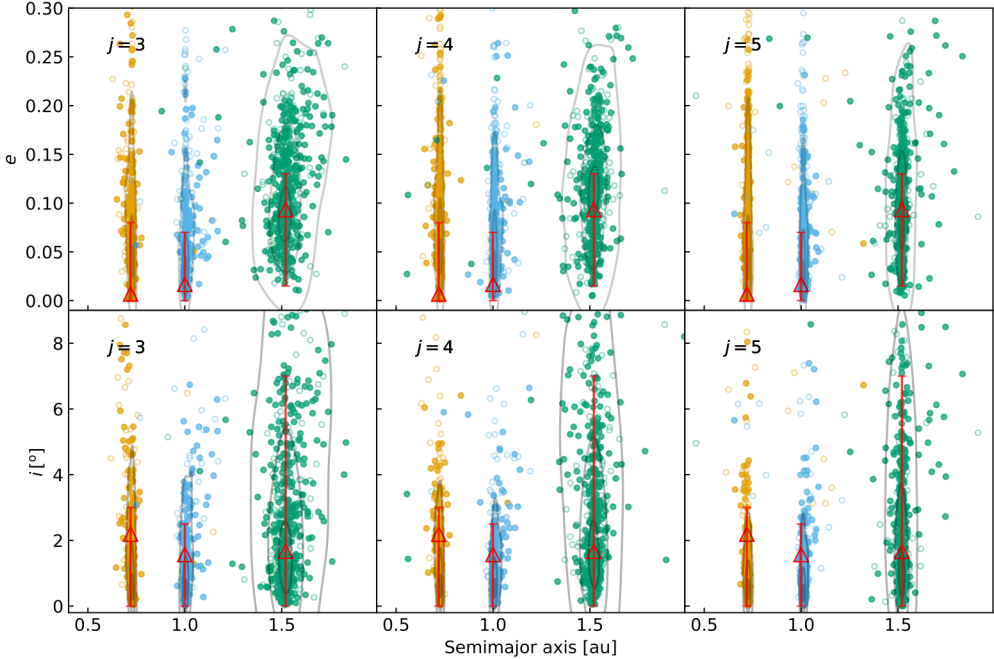


Figure 4.8. Dynamical properties for planet systems, in which Theia collides with Earth. The upper panels show the final eccentricities of Venus, Earth, and Mars, while the lower panels display their final inclinations relative to the invariable plane. Different scatter points are the results of the simulations that end up with Solar-like (solid dots) or other (open dots) systems (see Fig. 4.7 for definition). We overplot the median 10%, 50%, and 90% contours of the scatter. Each column corresponds to a different initial Venus-Mars resonance. For reference, we include the present-day eccentricities of the terrestrial planets and the inclinations (triangle) and the range of them on secular timescales (error bar) of the terrestrial planets (Ito & Tanikawa 2002).

sity profile. The width of the feeding zone is 6 times the planet Hill radius centered at the planet orbit (Lissauer 1993).

The planet formation simulation via the above planetesimal accretion is shown on the right panel of Fig. 4.6. All four embryos are initialized at the start, but at different locations. The ring-like distribution of planetesimals is centered at 1 au, promoting the growth of Venus and Earth. Therefore, they gain more mass than Theia and Mars. Finally, they consume all the planetesimals in their feeding zones, reaching the planetesimal isolation mass. The planets are born inside the 2:1 resonance. With slight migration, they are trapped in the 2:3:4:6 resonance chain.

Despite simplifying processes such as disk evolution and planetesimal scattering, and lacking exhaustive parameter exploration, these simulations reveal that both planetesimal and pebble accretion models yield resonant configurations comparable to the initial conditions of our post-disk N-body framework.

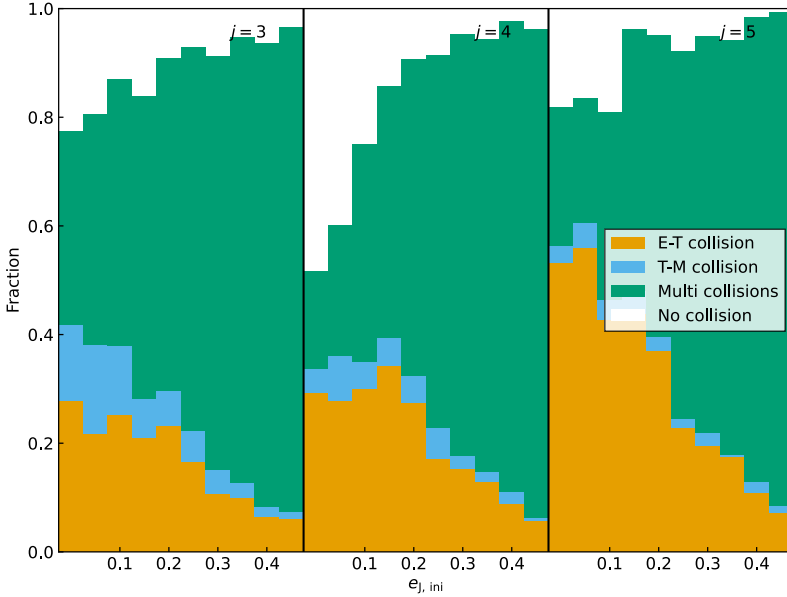


Figure 4.9. Statistical outcomes of the simulated Solar Systems and their dependence on initial conditions. The architecture of simulated systems is classified into four groups: 1) Theia collides with Earth (orange); 2) Theia collides with Mars (blue); 3) There are multiple collisions (green); 4) No collisions occurred within the end time of the simulation (white). The left, middle, and right panels display results for different initial resonances between Earth and Theia (the resonance number is shown at the top right of each panel). Within each panel, separate histograms represent simulation outcomes starting with different initial eccentricities for Jupiter.

4.B Parameter sensitivity

To assess how the properties of the simulated systems depend on the initial conditions, we systematically varied two key parameters: the initial eccentricity of Jupiter $e_{J,\text{ini}}$, and the initial resonance configuration between Earth and Theia, characterized by the resonance number j . In contrast to these parameters, our experiments show that the results are nearly insensitive to variations in the eccentricity damping parameter in the disk K_e and Saturn's outward migration timescale τ_S . The timescale of Saturn's outward migration τ_S is parameterized between 0.8 to 16 Myr. The eccentricity damping factor K_e is changed logarithmically in a range of evenly-spaced grids from 10^2 to 10^4 .

Naturally, varying the initial eccentricity of Jupiter affects its final eccentricity. In Fig. 4.7, we show the forced and free eccentricities from all our simulations. We change $e_{J,\text{ini}}$ in the range of 0 to 0.05 (linear grid). As $e_{J,\text{ini}}$ increases, both e_{forced} and e_{free} rise, with e_{free} exhibiting a more pronounced increase. For comparison, we also plot the observed value of Jupiter's eccentricity. Our results indicate that simulated systems align best with the Solar System when $e_{J,\text{ini}} < 0.02$.

We select the simulated systems with their final Jupiter eccentricity close to the present-day Jupiter. Those systems are labeled as "Solar-like systems", as highlighted by the circle in Fig. 4.7. The radius of the circle is 0.01. Then, the dynamical properties of the planets in the Solar-like systems are compared with those in the real Solar system. We already studied the angular momentum deficit (AMD), period ratio, impact velocity, and the timing

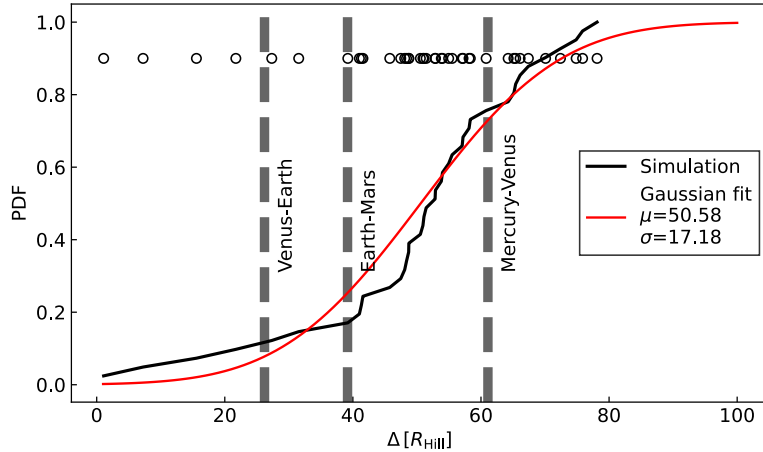


Figure 4.10. Cumulative distribution of the mutual separation (Δ) between each two adjacent terrestrial planets in the collisional growth scenario. The unit is the mutual Hill radius. The black curve shows the distribution of the simulation results. Each data point from the simulation is shown with the black circles. We use a Gaussian to fit the probability distribution, as shown in the red curve. The vertical dashed lines show the values from the terrestrial planets in the Solar system.

between Theia and Earth in the main text (Fig. 4.4). Here, the eccentricity and inclination of each terrestrial planet are shown in Fig. 4.8. The eccentricity and inclination values in our simulated systems are consistent with the secular evolution of the real Solar system. To give a full comparison, the information of those systems that are not Solar-like is also exhibited using open circles in Fig. 4.8. We also test three different initial architectures, corresponding to three different values of the resonance number $j = 3, 4, 5$ between Theia and Earth. As j increases, Theia stays in an orbit closer to the Earth. As a result, Mars experiences less close encounters with Theia and its semimajor axis is less dispersed.

Variations in the initial eccentricity of Jupiter, $e_{J,\text{ini}}$, lead to markedly different system architectures (see Fig. 4.9). A higher $e_{J,\text{ini}}$ more strongly perturbs the inner terrestrial planets via secular interaction, resulting in a higher frequency of multiple collision events. In contrast, when Jupiter starts on a nearly circular orbit, such violent interactions are less common. A higher fraction of systems only have one single collision or are even collision-free over the 100 Myr simulation period. In the systems that stayed collision-free, half have their resonance angles circulate. For those systems, we expect the planets to eventually collide. Otherwise, the terrestrial planets are still linked by the original resonance chain. As j increases, more and more simulated systems have Theia and Earth collisions (orange bars) while fewer have Theia colliding with Mars (blue bars). In Fig. 4.9, the number of collision-free systems increases when j increases from 3 to 4, due to the stronger resilience of the 5:4 resonance. As j increases to 5, the number of collision-free systems decreases again due to the instability triggered by too close orbits between Theia and Earth (Petit et al. 2020).

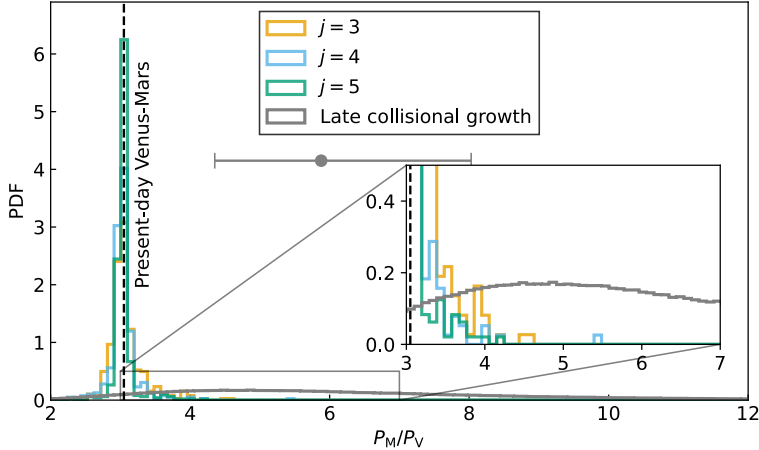


Figure 4.11. Mars-Venus period ratio probability distribution from different models. Similar to Fig. 4.3, here we zoom in to display the shape of the period ratio distribution resulting from the late formation scenario (grey histogram). The median 50% range and the median value of the late formation distribution are indicated by the error bar and its center value. We zoom in on the plot in the inset such that the peak of the period ratio distribution in the late formation scenario is visualized.

4.C Venus-Mars period ratio in the late collisional growth scenario

While exhibiting the properties of simulated systems in our early formation scenario, we also compare the Venus-Mars period ratio with that from the late formation scenario. In such a case, planets are formed by the collisional growth between planetesimals and Mars-sized embryos.

The simulation setups for the late collisional growth scenario are the same as those used in Kokubo et al. (2025). We give a brief description here. The simulations start with 15 protoplanets of equal mass, each with $m = 0.15 m_{\oplus}$. Their semimajor axes are distributed between 0.5 and 1.5 au, with adjacent protoplanets separated by 10 times the mutual Hill radius. The initial eccentricities and inclinations follow Rayleigh distributions with dispersions of $\sigma_e = 0.01$ and $\sigma_I = 0.005$. Each body is assumed to have a mean bulk density of 3 g cm^{-3} . In total, 20 independent simulations are performed.

The dynamical evolution of the system is computed using a modified Hermite integrator, as described by Kokubo et al. (2025), which efficiently resolves close encounters while ensuring accurate energy conservation in gravitational N-body simulations. To accelerate the simulation, a block timestep scheme has been adopted (Makino 1991). Perfect accretion is assumed when two planets collide, conserving both mass and momentum. Each simulation runs for 1.7×10^2 Myr.

We here calculate the separation between each pair of adjacent planets at the end of the 20 simulations, and the results are shown in Fig. 4.10. This figure shows the distribution of the post-giant impact semi-major axes difference among the planets in units of the mutual Hill radius (Δ). Systems with close-to-zero Δ are allowed (stable) due to their large mutual inclinations, $\sim 10^\circ$. The separations among the terrestrial planets in the Solar system are also indicated. The simulated distribution of separations closely matches the values observed in

the Solar system. We find that the probability distribution peaks around 50 Hill radii. To fit this distribution, we use a Gaussian profile. The best fit to the distribution in Δ is given by a mean value of $\mu = 50.58$ and a standard deviation $\sigma = 17.18$.

Using this separation distribution, we apply the Monte Carlo method to generate a distribution of the period ratio between Venus and Mars. We generate two sets of separation distances: one covering the Venus-Earth pair and the other for the Earth-Mars pair, assuming that $\Delta \sim \mathcal{N}(\mu, \sigma)$ for each of them. The set of synthetic Δ is then converted back into period ratios, and the resulting distribution is shown in Fig. 4.3. Figure 4.11 provides the same information, but with an extended period ratio. The peak of the period ratio distribution of the late formation scenario (≈ 4.9) is about twice that of the present-day value (3.05). Statistically, only the lower 10% percentile covers the real Mars-Venus period ratio of 3.05. More detailed analysis will be presented in (Kokubo et al. 2025) in the context of dynamical stability criteria for Kepler planet systems.

904.C. VENUS-MARS PERIOD RATIO IN THE LATE COLLISIONAL GROWTH SCENARIO